
Zero-Shot Mono-to-Binaural Speech Synthesis

Alon Levkovich
Google Research
alevkovitch@google.com

Julian Salazar
Google DeepMind
julsal@google.com

Soroosh Mariooryad
Google DeepMind
soroosh@google.com

RJ Skerry-Ryan
Google DeepMind
rjryan@google.com

Nadav Bar
Google Research
nadavbar@google.com

Bastiaan Kleijn
Google Research
kleijnb@google.com

Eliya Nachmani
Google Research
eliyn@google.com

Abstract

We present ZeroBAS, a neural method to synthesize binaural audio from monaural audio recordings and positional information *without training on any binaural data*. To our knowledge, this is the first published zero-shot neural approach to mono-to-binaural audio synthesis. Specifically, we show that a parameter-free geometric time warping and amplitude scaling based on source location suffices to get an initial binaural synthesis that can be refined by iteratively applying a pre-trained denoising vocoder. Furthermore, we find this leads to generalization across room conditions, which we measure by introducing a new dataset, TUT Mono-to-Binaural, to evaluate state-of-the-art monaural-to-binaural synthesis methods on unseen conditions. Our zero-shot method is perceptually on-par with the performance of supervised methods on the standard mono-to-binaural dataset [Richard et al., 2021], and even surpasses them on our out-of-distribution TUT Mono-to-Binaural dataset. Our results highlight the potential of pretrained generative audio models and zero-shot learning to unlock robust binaural audio synthesis.

1 Introduction

Humans possess a remarkable ability to localize sound sources and perceive the surrounding environment through auditory cues alone. This sensory ability, known as *spatial hearing*, plays a critical role in numerous everyday tasks, including identifying speakers in crowded conversations and navigating complex environments. Hence, emulating a coherent sense of space via listening devices like headphones becomes paramount to creating truly immersive artificial experiences. Due to the lack of multi-channel and positional data for most acoustic and room conditions, the robust and low/zero-resource synthesis of binaural audio from single-source, single-channel (mono) recordings is a crucial step towards advancing augmented reality (AR) and virtual reality (VR) technologies.

Conventional mono-to-binaural synthesis techniques leverage a digital signal processing (DSP) framework. Within this framework, the head-related transfer function (HRTF), the room impulse response (RIR), and ambient noise are modeled as linear time-invariant (LTI) systems [Savioja et al., 1999, Zotkin et al., 2004, Sunder et al., 2015, Zhang et al., 2017]. These DSP-based approaches are prevalent in commercial applications due to their established theoretical foundation and their ability to generate perceptually realistic audio experiences. However, real acoustic propagation, unlike the one modeled by LTI systems, has nonlinear wave effects. Recent advancements in the field

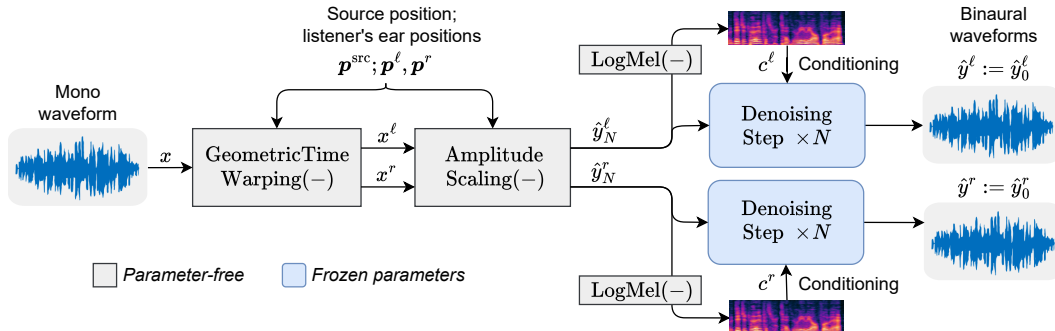


Figure 1: Our proposed ZeroBAS method. Mono waveform is binauralized with geometric time warping conditional on the speaker’s position, then the two channels’ amplitudes are scaled. Each channel is then denoised $N = 3$ times by a low noise-level step of a monaural denoising vocoder.

have witnessed a paradigm shift towards employing machine learning methods via the paradigm of supervised learning [Richard et al., 2021, Huang et al., 2022, Leng et al., 2022, Lee and Lee, 2023, Liu et al., 2023, Chen et al., 2023a].

The task of synthesizing binaural audio from monophonic sources presents a significant challenge for supervised learning models. This difficulty stems from two primary limitations: (1) the scarcity of position-annotated binaural audio datasets, and (2) the inherent variability of real-world environments, characterized by diverse room acoustics and background noise conditions. Data collection for supervised learning necessitates specialized equipment, including tracking systems and binaural recording devices, which are both cost-prohibitive and often unavailable. Moreover, supervised models are susceptible to overfitting on the specific rooms, speaker characteristics, and languages in the training data, especially when the data is small (the standard dataset of Richard et al., 2021 is only two hours). To address these limitations, we propose a novel zero-shot approach for monaural-to-binaural synthesis that is effective across a broader spectrum of recording scenarios by leveraging a monaural vocoder trained on tens of thousands of hours. Our contributions are:

- The first zero-shot method for neural mono-to-binaural audio synthesis, leveraging geometric time warping, amplitude scaling, and a (monaural) denoising vocoder [WaveFit; Koizumi et al., 2022a]. Notably, we achieve natural binaural audio generation that is perceptually on par (MOS, MUSHRA) with existing supervised methods despite never seeing binaural data.
- A novel dataset-building approach and dataset, TUT Mono-to-Binaural, derived from the location-annotated ambisonic recordings of speech events in the TUT Sound Events 2018 dataset [Adavanne et al., 2019]. When evaluated on this out-of-distribution data, past supervised methods degrade significantly while ZeroBAS continues performing well.
- A mathematical discussion of the expected phase and amplitude errors of synthesised binaural waveforms in the high-error regime. We find that phase and amplitude errors are $\pi/2$ and ε (the distance between the ground truth and the estimation), which we connect to our experimental results that empirically validate these derivations.

2 Related Work

DSP techniques approach the mono-to-binaural problem as a stack of acoustic components, each of which is an LTI system. Accurate wave-based simulation of RIRs is computationally expensive, and thus most real-time systems rely on simplified geometrical models [Välimäki et al., 2012, Savioja et al., 1999]. HRTFs need to be recorded inside an anechoic chamber in about 10k locations for good results [Li and Peissig, 2020]. DSP approaches treat these functions as a series of convolutions that are applied to the input signal.

Richard et al. [2021] proposed one of first uses of neural networks for mono-to-binaural synthesis, composing a neural time-warping module (WarpNet) and a temporal (hyper-)convolutional neural network (CNN) to learn a direct map between mono and binaural waveforms. BinauralGrad [Leng

et al., 2022] was the first to use a denoising diffusion probabilistic model (DDPM), composed of two stages: the first produces a channel-averaged waveform, then the second conditions on this, the original data, and its geometric warpings to denoise both channels of binaural audio.

Since then, better incorporation of the inductive biases from DSP have led to more efficient neural systems. Neural Fourier Shift [NFS; Lee and Lee, 2023] predicts delays and scaling from speaker locations and achieve close to state-of-the-art performance with a significantly smaller model. DopplerBAS [Liu et al., 2023] found that incorporating the Doppler effect into the conditioning features improved the phase loss of both the WarpNet and BinauralGrad systems. Kitamura and Itou [2023] used a structured state space sequence (S4) model for the mono-to-binaural task and showed that this type of model can create high quality binaural audio. Huang et al. [2022] show that mono-to-binaural audio synthesis can be performed end to end with the use of audio codes. Motivated by the difficulty of collecting HRTF and RIR data, Gebru et al. [2021] showed that an implicit HRTF can be learned by a temporal CNN. Richard et al. [2022] and Lee et al. [2022] showed that deep neural networks can be used to artificially estimate RIR filters from training data. Luo et al. [2022] created a model for learning an implicit representation of an acoustic field, which can be then applied to create spatial audio. Furthermore, a different line of work uses visual conditioning for the generation of binaural audio [Xu et al., 2021, Parida et al., 2022, Chen et al., 2023b, Liang et al., 2023, Somayazulu et al., 2023, Garg et al., 2021, Yoshida et al., 2023, Xu et al., 2023].

3 Approach

Our proposed zero-shot mono-to-binaural synthesis method utilizes a three-stage architecture. The first stage follows previous work and performs geometric time warping (GTW) to manipulate the input mono waveform into two channels based on the provided position information. Subsequently, our proposed amplitude scaling (AS) module adjusts the amplitude of the warped signal. Finally, an existing denoising vocoder iteratively refines the processed signal to generate the binaural output composed of two channels. Figure 1 provides a visual representation of this pipeline.

Let x denote the mono source signal. Its position at time t is given by the 3D vector $\mathbf{p}_t^{\text{src}}$. Let ℓ and r correspond to the listener’s left and right ear. Their positions at t are given by 3D vectors $\mathbf{p}_t^\ell, \mathbf{p}_t^r$. The system first applies GTW to x conditioned on $\mathbf{p}_t^{\text{src}}, \mathbf{p}_t^\ell$ and \mathbf{p}_t^r . This warping gives left and right preprocessed channels, denoted by x^ℓ and x^r . Then, AS is employed jointly on x^ℓ and x^r , conditioning on the same data. This step aims to further enhance the spatial perception of the signal. The resulting intermediate left and right channels are denoted by \hat{x}^ℓ and \hat{x}^r , respectively.

Finally, the denoising step sets its noisy inputs $\hat{y}_N^\ell, \hat{y}_N^r$ to be the outputs of the previous stage, \hat{x}^ℓ, \hat{x}^r . This replaces the typical Gaussian noise initialization used when training or sampling from denoising models. $\hat{y}_N^\ell, \hat{y}_N^r$ are fed separately into the same pretrained denoising vocoder, which treats each waveform as mono audio. The temporal sequences of conditioning vectors $\mathbf{c}^\ell, \mathbf{c}^r$ are obtained by extracting the log-mel features of \hat{x}^ℓ, \hat{x}^r . A low noise level k is also conditioned on, to reflect that we are emulating an input that is “close” to a true binaural sample. In the case of our denoising vocoder, WaveFit [Koizumi et al., 2022a], this noise level is given by a choice of conditioning timestep; specifically, the last timestep of the WaveFit training’s denoising process. This sampling is repeated for N iterations. The full algorithm is shown in Algorithm 1.

In the Experiments section, we show that our approach produces a binaural speech rendering whose quality approximates the ground truth binaural audio. Note that our method does not take into account room effects nor the listener’s head shape. Thus, we produce spatial audio which imputes both a generalized low RIR room (regularized by all the data the vocoder was trained on), and an implicit HRTF.

3.1 Geometric Time Warping (GTW)

GTW aims to estimate a warfield that separates the left and right binaural signals by applying the interaural time delay (ITD) based on the relative positions of the sound source and the listener’s ears. Richard et al. [2021] proposed GTW as a method to generate an initial estimate of the perceived signals. This approach offers a simple and parameter-free solution for warfield which can be applied to the mono signal. Let S denote the signal’s sample rate and ν_{sound} represent the speed of sound. The system employs basic GTW on the monaural signal x . This warping is achieved by computing a

Algorithm 1 ZeroBAS, our zero-shot mono-to-binaural algorithm:

Require: Denoising vocoder \mathcal{V}_θ , iteration count N , low noise level k , and the following temporal sequences: mono waveform x , speaker position \mathbf{p}^{src} , listener’s ear locations $\mathbf{p}^\ell, \mathbf{p}^r$.

$$x^\ell, x^r = \text{GeometricTimeWarping}(x, \mathbf{p}^{\text{src}}, \mathbf{p}^\ell, \mathbf{p}^r)$$

$$\hat{x}^\ell, \hat{x}^r = \text{AmplitudeScaling}(x^\ell, x^r, \mathbf{p}^{\text{src}}, \mathbf{p}^\ell, \mathbf{p}^r)$$

$$\mathbf{c}^\ell, \mathbf{c}^r = \text{LogMel}(\hat{x}^\ell), \text{LogMel}(\hat{x}^r)$$

$$\hat{y}_N^\ell, \hat{y}_N^r := \hat{x}^\ell, \hat{x}^r$$

for $i \leftarrow N$ to 1 **do**

$$\hat{y}_{i-1}^\ell, \hat{y}_{i-1}^r = \mathcal{V}_\theta(\hat{y}_i^\ell, \mathbf{c}^\ell, k), \mathcal{V}_\theta(\hat{y}_i^r, \mathbf{c}^r, k)$$

end for

return $\hat{y}^\ell, \hat{y}^r := \hat{y}_0^\ell, \hat{y}_0^r$.

warfield for both the left and right listening channels, denoted by $\rho^\ell(t), \rho^r(t)$. The values of this warfield are computed using on the source and listener ear positions $\mathbf{p}_t^{\text{src}}, \mathbf{p}_t^\ell, \mathbf{p}_t^r$:

$$\rho^\ell(t) := t - \frac{S}{\nu_{\text{sound}}} \|\mathbf{p}_t^{\text{src}} - \mathbf{p}_t^\ell\|_2, \quad \rho^r(t) := t - \frac{S}{\nu_{\text{sound}}} \|\mathbf{p}_t^{\text{src}} - \mathbf{p}_t^r\|_2 \quad (1)$$

As this function takes non-integer values, we can define the warped left and right signals \hat{x}^ℓ, \hat{x}^r with respect to the original indexing t via linear interpolation:

$$x_t^\ell := (\lceil \rho^\ell(t) \rceil - \rho^\ell(t)) \cdot x_{\lfloor \rho^\ell(t) \rfloor} + (\rho^\ell(t) - \lfloor \rho^\ell(t) \rfloor) \cdot x_{\lceil \rho^\ell(t) \rceil},$$

$$x_t^r := (\lceil \rho^r(t) \rceil - \rho^r(t)) \cdot x_{\lfloor \rho^r(t) \rfloor} + (\rho^r(t) - \lfloor \rho^r(t) \rfloor) \cdot x_{\lceil \rho^r(t) \rceil}.$$

3.2 Amplitude Scaling (AS)

In addition to manipulating the time-delay of the signal, we also manipulate the amplitude of the signal based on the position of the speaker. Human spatial perception of sound relies on various factors, including the ITD, the interaural level difference (ILD), and spectral cues due to HRTFs. While prior works [Wersényi, 2010, Baumgarte and Faller, 2003] suggest that the ILD is mostly caused by scattering off of the head and is dominant in human spatial perception for sounds with high frequencies, we find that amplitude scaling based on the inverse square law has a positive effect on the perceived spatial accuracy of the processed signal.

Our approach aims to leverage this amplitude manipulation to enhance the spatial realism of the generated binaural audio. Let D be the Euclidean distance from the origin of the sound waves. Then by the inverse-square law, pressure drops at a $1/D^2$ ratio [Zahorik et al., 2005]. In the case of microphones, pressure manifests as amplitude. Acknowledging that the left-right microphone distance of the KEMAR mannequin used in datasets like Richard et al. [2021]’s is only an approximation of human heads, we define:

$$D_t^\ell = \|\mathbf{p}^{\text{src}} - \mathbf{p}_t^\ell\|_2, \quad D_t^r = \|\mathbf{p}^{\text{src}} - \mathbf{p}_t^r\|_2. \quad (2)$$

Then, at each time step we scale down the magnitude of the side furthest from the source, using the ratio of the closer side’s distance versus the further side’s distance:

$$\hat{x}_t^\ell := \min(1, (D_t^r/D_t^\ell)^2) \cdot x_t^\ell, \quad \hat{x}_t^r := \min(1, (D_t^\ell/D_t^r)^2) \cdot x_t^r. \quad (3)$$

3.3 Denoising Vocoder

GTW and AS are simple, parameter-free operations that only roughly approximate binaural audio; using the warped and scaled speech signals \hat{x}^ℓ, \hat{x}^r as-is results in acoustic artifacts and inconsistencies. Hence, there is a need for further refinement to generate natural-sounding binaural audio. To this end, we propose that a sufficiently well-trained denoising vocoder could be used on each signal *independently*. We use a WaveFit neural vocoder [Koizumi et al., 2022a] as our denoising vocoder model. It is a fixed-point iteration vocoder that takes the denoising perspective of DDPMs [Ho et al., 2020]; and takes the discriminator of generative adversarial networks, specifically MelGAN’s [Kumar et al., 2019], to learn a sampling-free iterable map that can generate natural speech from a degraded

input speech signal. As a vocoder, it takes log-mel spectrogram features and noise as input and produces clean waveform output. In WaveFit’s notation, we perform the iterated application of

$$\hat{y}_{i-1} := \mathcal{V}_\theta(\hat{y}_i, \mathbf{c}, k) := \mathcal{G}(\hat{y}_i - \mathcal{F}_\theta(\hat{y}_i, \mathbf{c}, k), \mathbf{c}), \quad (4)$$

where \mathbf{c} is the spectrogram to convert and \hat{y}_{i-1} is a candidate waveform refined from \hat{y}_i . \mathcal{G} is a parameter-free gain adjustment operator and \mathcal{F}_θ is the WaveGrad architecture [Chen et al., 2021] trained for reconstruction under a discriminator.

At training time, the starting noise is given by $\hat{y}_K \sim \mathcal{N}(0, \Sigma_{\mathbf{c}})$ where $\Sigma_{\mathbf{c}}$ is a covariance matrix initialized as in SpecGrad [Koizumi et al., 2022b] to capture the spectral envelope of \mathbf{c} ; both k, i iterate over $K, \dots, 1$. Then, at inference time, we express our “approximation” hypothesis by iterating at the noise level of WaveFit’s final denoising step ($k = 1$). We then iteratively denoise $\hat{y}_N^l, \hat{y}_N^r := \hat{x}^l, \hat{x}^r$, conditioning on their initial log-mel spectrograms and the fixed low noise level for steps $i = N, \dots, 1$.

4 Phase and Amplitude Error Analysis

This section provides an error analysis for phase and amplitude estimation, adopting the notation from Richard et al. [2021]. Here, Y represents the audio signal in the frequency domain, and \hat{Y} its prediction, with ε denoting the distance between them. The analysis distinguishes between high- and low-error regimes, defined by $\varepsilon/|\hat{Y}| \gg 1$ and $\varepsilon/|\hat{Y}| \ll 1$, respectively. In the high-error regime, Lemma 1 demonstrates a phase error of $\pi/2$ and an amplitude error of ε . In Table 5 we see that numerical results on the TUT dataset align with the high-error approximation of the phase error, $\pi/2$. Since the error surface is monotonic, this suggests all methods are in the high-error regime, which is consistent with no method having seen the TUT dataset.

Figure 2 presents a comparison between the exact expected errors (via evaluating the integrals) with the high-error approximations of Lemma 1. Focusing on the high-error regime, starting at $15 < \varepsilon/|\hat{Y}|$ (bottom-right regions of each figure), we see that the amplitude error, shown in Figures 2(a) and 2(b), demonstrates a strong agreement between the expected errors and our theory. This validates Lemma 1, confirming that the amplitude error is proportional to ε , which is intuitively consistent as ε is the distance between Y and \hat{Y} . Also, in this region of Figures 2(c) and 2(d) the phase error is predominantly $\pi/2$, aligning with the prediction of Lemma 1. For completeness, a theoretical analysis for the low error regime, where $\varepsilon/|\hat{Y}| \ll 1$, is provided in Lemma 2 in the Appendix.

Lemma 1. *Let $\hat{Y} \in \mathbb{C}$, and let there be a sphere of complex numbers with distance ε from \hat{Y} such that $Y \in \mathbb{S}_\varepsilon = \{Y \in \mathbb{C} : |Y - \hat{Y}| = \varepsilon\}$. Assuming a high (relative) error regime $\frac{\varepsilon}{|\hat{Y}|} \gg 1$, the expected phase and amplitude error can be expressed as:*

$$(a) \quad \mathbb{E}_Y \left(\mathcal{L}^{(phase)}(Y, \hat{Y}) \right) \approx \frac{\pi}{2}, \quad (b) \quad \mathbb{E}_Y \left(\mathcal{L}^{(amp)}(Y, \hat{Y}) \right) \approx \varepsilon. \quad (5)$$

Proof. This follows from Lemma 1 of [Richard et al., 2021] combined with first-order approximations induced by large error; see Appendix. \square

5 Experiments

5.1 Data and Models

For our experiments we use two datasets. The first is the Binaural Speech dataset¹ released by Richard et al. [2021]. The dataset contains paired mono and binaural audio with tracking information, jointly collected in a non-anechoic room; see Richard et al. [2021] for more details. The second dataset is an adapted version of TUT Sound Events 2018² [Adavanne et al., 2019] which we name "TUT Mono-to-Binaural". It contains 1,174 recordings, each about 2 seconds long. Overall, there are 2.15

¹<https://github.com/facebookresearch/BinauralSpeechSynthesis/releases/tag/v1.0>

²<https://zenodo.org/records/1237703>

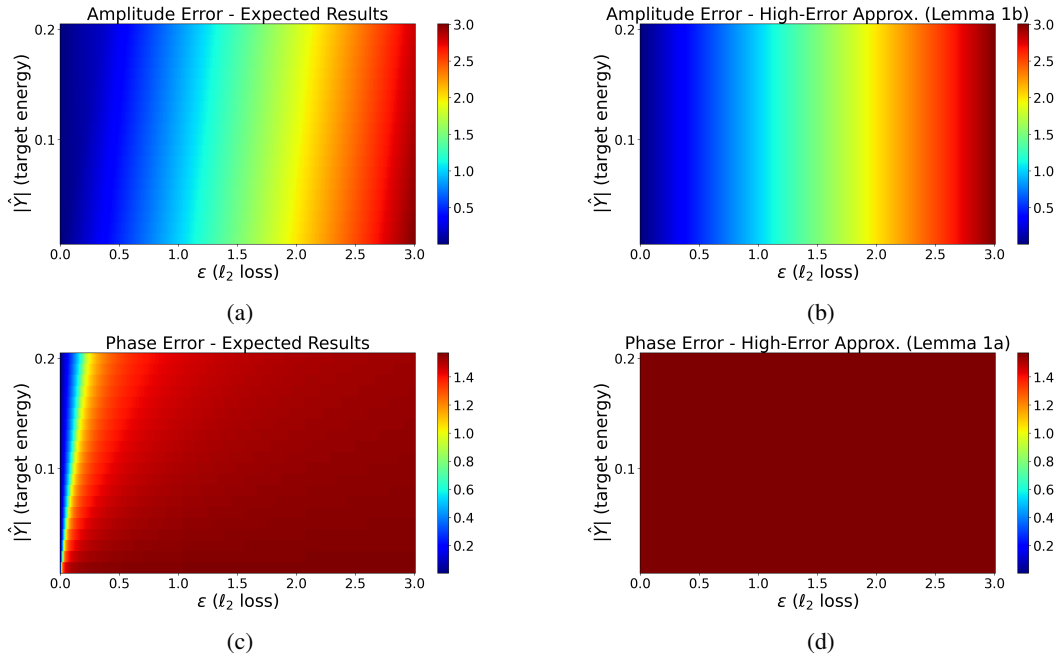


Figure 2: Comparison between the expected errors from Richard et al. [2021] and our Lemma 1. (a) and (b) depict the expected amplitude error and our high-error regime approximation, respectively, while panels (c) and (d) illustrate the same for phase error.

hours of recordings in the dataset. The spoken language is French, speakers are recorded in a studio, and each recording is played in a single location. Using this dataset ensures a zero-shot evaluation for all of the methods tested in this paper, as none were trained on this data. For our DSP baseline, we use the open-source Resonance Audio package.³ This package takes speaker and listener locations, room size, and room materials as input. The WaveFit vocoder is described in Koizumi et al. [2022a]. The pretrained weights we use were trained on the 60k-hour LibriLight audiobook dataset [Kahn et al., 2020] using 128 v3 TPUs for 500k steps; hyperparameters are as described in Koizumi et al. [2022a].

5.1.1 TUT Mono-to-Binaural: Dataset Construction

Our purpose in creating and using the TUT mono-to-binaural dataset is threefold: (a) to demonstrate a new approach for creating mono-to-binaural synthesis datasets due to their scarcity, (b) to evaluate the ability of different methods to generalize to different rooms and acoustic environments, and (c) to evaluate the ability of different methods to generalize to different speakers. The TUT Sound Events 2018 is built for sound event localization and is composed of anechoic first-order ambisonic recordings from the DCASE 2016, Task 2 dataset⁴ [Lafay et al., 2017]. In TUT Sound Events 2018, mono recordings were played back using a loudspeaker at distances ranging from 1-10 meters and captured by an ambisonic microphone. Sound event locations are given using azimuth, elevation and distance, with each sound event having a single location.

Starting from this data, we apply several processing steps: First, the speaker location information provided in azimuth, elevation, and distance were converted into a Cartesian coordinate system (x, y, z) to align with previous work like Richard et al. [2021]. Next, ground-truth metadata was leveraged to cut out speech segments from the recordings using their provided timestamps. To generate the binaural ground truth for our evaluation, ambisonic recordings are converted to binaural audio using OmniTone⁵, a well-established commercial DSP ambisonic decoder with a binaural renderer. Finally, the corresponding original monaural recordings are obtained from the DCASE

³<https://github.com/resonance-audio>

⁴https://archive.org/details/dcase2016_task2_train_dev

⁵<https://googlechrome.github.io/omnitone/#home>

Table 1: Objective and subjective evaluations of models on the Binaural Speech dataset.

TYPE	MODEL	WAVE ℓ_2 (\downarrow)	AMP ℓ_2 (\downarrow)	PHASE ℓ_2 (\downarrow)	$\mathcal{L}_{\text{STFT}}$ (\downarrow)	MOS (\uparrow)
ZERO-SHOT	DSP (OURS)	0.812	0.052	1.572	1.91	3.84 \pm 0.19
	ZEROBAS (OURS)	0.440	0.053	1.508	1.91	4.07 \pm 0.17
SUPERVISED	WARPNET	0.179	0.037	0.968	1.52	3.86 \pm 0.16
	BINAURALGRAD	0.128	0.030	0.837	1.25	4.01 \pm 0.14
	NFS	0.172	0.035	0.999	1.29	3.99 \pm 0.15
GROUND TRUTH	-	-	-	-	-	4.30 \pm 0.12

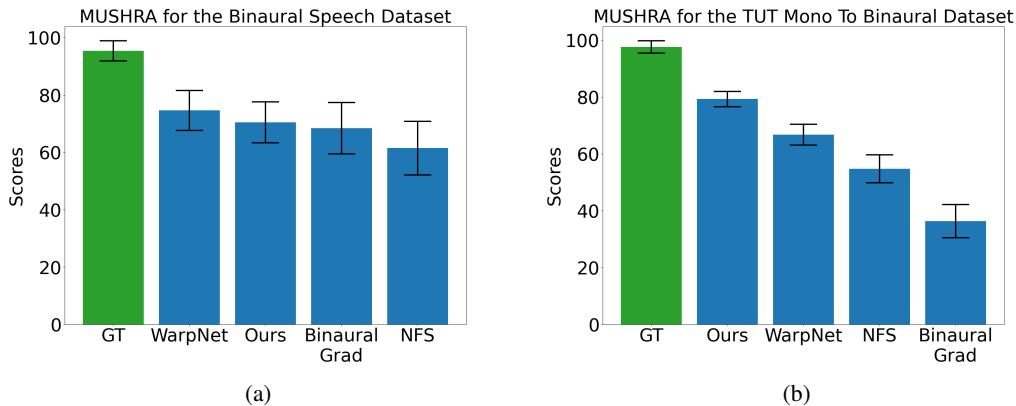


Figure 3: MUSHRA results for (a) Binaural Speech dataset and (b) TUT Mono-to-Binaural dataset.

2016, Task 2 dataset. Note that unlike the Binaural Speech Dataset, these mono recordings are recorded separately from their ambisonic re-recordings and binaural renderings.

5.2 Evaluations

For objective evaluations, we use metrics found in prior work. **Wave ℓ_2** : mean squared error (MSE) between the ground truth and synthesized per-channel waveforms. This metric is multiplied by 10^3 . **Amplitude ℓ_2** : MSE between the STFTs of the ground truth and synthesized audio, with respect to amplitude. **Phase ℓ_2** : MSE between the left - right phase angle of the ground truth and synthesized audio. Phase is computed from the STFT. **MRSTFT $\mathcal{L}_{\text{STFT}}$** is the multi-resolution spectral loss.

For subjective evaluations, we perform **MOS** and **MUSHRA** evaluations. For MOS, we collect mean opinion scores towards axes of naturalness. Human evaluators are tasked with assigning a rating on a five-point scale to denote the perceived naturalness of a given speech utterance, spanning from 1 (indicative of poor quality) to 5 (indicative of excellent quality). For every experiment, we use 50 random samples from each method. Every example is rated 5 times by different raters, with each experiment participated in by at least 30 raters. In the MUSHRA (multiple stimuli with hidden reference and anchor) evaluation, each question first presents the binaural recordings from the test set as a reference. The human raters are asked to rate how similar each model output is to the reference on a scale from 0 to 100. The samples include a hidden reference as an anchor, and the outputs of the models appear in random permutation order. For this test we used 50 random samples from each method. Following the MUSHRA protocol⁶, we discard raters who gave >15% of hidden references a score below 90. We used the model and code releases of WarpNet⁷, BinauralGrad⁸, and NFS⁹ to synthesize audio for subjective evaluations of these systems.

⁶https://www.itu.int/dms_pubrec/itu-r/rec/bs/R-REC-BS.1534-3-201510-I!!PDF-E.pdf

⁷<https://github.com/facebookresearch/BinauralSpeechSynthesis>

⁸<https://github.com/microsoft/NeuralSpeech/tree/master/BinauralGrad>

⁹<https://github.com/jin-woo-lee/nfs-binaural>

Table 2: Objective and subjective evaluations of models on the TUT Mono-to-Binaural dataset.

TYPE	MODEL	WAVE ℓ_2 (\downarrow)	AMP ℓ_2 (\downarrow)	PHASE ℓ_2 (\downarrow)	$\mathcal{L}_{\text{STFT}}$ (\downarrow)	MOS (\uparrow)
ZERO-SHOT	DSP (OURS)	1.134	0.075	1.572	2.93	3.09 \pm 0.28
	ZEROBAS (OURS)	0.293	0.045	1.572	2.93	3.98 \pm 0.15
SUPERVISED	WARPNET	2.909	0.099	1.571	6.66	3.60 \pm 0.26
	BINAURALGRAD	3.228	0.218	1.571	5.40	3.27 \pm 0.32
	NFS	1.574	0.085	1.571	3.06	3.79 \pm 0.23
GROUND TRUTH	-	-	-	-	-	4.08 \pm 0.11

5.3 Binaural Speech Dataset Results

In Table 1, we observe that ZeroBAS achieves significant objective improvements over the DSP baseline, despite not modeling additional interactions between the two generated channel streams or the RIR and HRTFs. Furthermore, the performance of ZeroBAS approaches that of the supervised methods, even though ZeroBAS has not been trained on the Binaural Speech dataset. In terms of Wave ℓ_2 , ZeroBAS under-performs the supervised methods WarpNet, BinauralGrad and NFS only by margins of 0.261, 0.312 and 0.268 respectively. In Amplitude ℓ_2 , ZeroBAS had an increase of 0.016, 0.023 and 0.018 with respect to WarpNet, BinauralGrad and NFS. For MRSTFT, there is a gap of 0.38, 0.66 and 0.62 in favor of WarpNet, BinauralGrad and NFS. With respect to Phase ℓ_2 , ZeroBAS has a large margin versus the supervised methods. Unlike supervised approaches, ZeroBAS inherently cannot model certain imperceptible artifacts present in the ground truth recordings. These artifacts, such as high-frequency noise introduced by recording equipment, can be implicitly captured by supervised methods, potentially leading to improved performance on objective metrics.

The subjective evaluation results in Table 1 show that ZeroBAS sounds slightly more natural to human raters than the supervised methods while being on par with them in the MUSHRA evaluation. ZeroBAS improves in MOS over WarpNet, BinauralGrad and NFS by 0.21, 0.06 and 0.08. MUSHRA results show that human raters do not have a statistically significant preference for any of the methods WarpNet, BinauralGrad, NFS or ZeroBAS. The ZeroBAS system leverages a WaveFit model trained on high-quality studio recordings which ensures the generated audio exhibits minimal artifacts and noise compared to binaural recordings, leading to improved perceptual quality for human listeners. The combination of objective (spatial audio evaluation) and subjective (high audio quality evaluation) assessments demonstrates ZeroBAS’s capability to achieve both spatial fidelity and listener preference. Samples can be heard in our demo page.

5.4 TUT Mono-to-Binaural Results

Although the zero-shot method underperforms supervised methods in the subjective evaluation on the Binaural Speech dataset, we argue that the supervised methods are sensitive to the room and recording conditions of the Binaural Speech dataset. To demonstrate this, we evaluated all method on our newly constructed TUT mono to binaural dataset. Table 5 demonstrates that our zero-shot method, ZeroBAS, significantly outperforms all supervised methods on the TUT mono to binaural dataset. In terms of Wave ℓ_2 error, the margin of improvement is large, with ZeroBAS surpassing supervised methods like WarpNet, BinauralGrad, and NFS by 2.616, 2.935, and 1.281. For Amplitude ℓ_2 error, ZeroBAS exhibits improvements of 0.54, 0.173, and 0.04 points compared to WarpNet, BinauralGrad, and NFS, respectively. In MRSTFT, ZeroBAS outperforms WarpNet, BinauralGrad, and NFS with 3.73, 2.74 and 0.13 points. Both ZeroBAS and the supervised methods struggle to capture accurate phase information, as evidenced by the Phase ℓ_2 metric. In addition, the results of the Phase ℓ_2 metric are consistent with our theoretical analysis in Lemma 1.

The subjective evaluation results presented in Table 5 further demonstrate that ZeroBAS exhibits superior performance in terms of perceived naturalness compared to the supervised methods WarpNet, BinauralGrad, and NFS. As evidenced by the Mean Opinion Score (MOS), ZeroBAS surpasses these methods by notable margins: 0.37, 0.70, and 0.18, respectively. Considering the confidence intervals, these results indicate that human listeners on the TUT mono to binaural dataset perceive ZeroBAS as more natural-sounding than the supervised methods, with its score approaching that of the ground truth recordings. Furthermore, MUSHRA evaluations reveal a statistically significant preference

Table 3: Ablation of our zero-shot method on the mono to binaural dataset

MODEL	WAVE ℓ_2 (\downarrow)	AMPLITUDE ℓ_2 (\downarrow)	PHASE ℓ_2 (\downarrow)	MOS (\uparrow)
ZEROBAS	0.440	0.053	1.508	4.07 \pm 0.17
w/o AS	0.802	0.059	1.539	2.93 \pm 0.16
w/o GTW	0.627	0.053	1.569	3.64 \pm 0.15
w/o AS, GTW	0.816	0.051	1.567	4.13 \pm 0.18
w/o WAVEFIT	0.539	0.044	1.572	3.52 \pm 0.16
DECODE FROM NOISE	0.495	0.065	1.534	2.50 \pm 0.16
WAVEFIT THEN WARPING	0.474	0.072	1.277	3.85 \pm 0.19
1 ITERATION	0.459	0.069	1.393	3.62 \pm 0.20
2 ITERATIONS	0.450	0.061	1.492	3.83 \pm 0.24
4 ITERATIONS	0.445	0.053	1.502	3.94 \pm 0.18
5 ITERATIONS	0.449	0.053	1.494	4.05 \pm 0.15

for the proposed ZeroBAS method compared to supervised approaches. This suggests that human listeners perceive the spatial quality of binaural signals generated by ZeroBAS to be superior.

Evaluation of existing supervised learning methods on the TUT mono-to-binaural dataset revealed several limitations. BinauralGrad produced outputs with substantial Gaussian noise, hindering the diffusion process’s convergence to clean signals for out-of-distribution samples. WarpNet and NFS exhibited two key failure modes: (a) Inability to retain speaker voice characteristics in the binaural output, leading to fidelity degradation, and (b) incorrect spatialization, manifesting as generated binaural speech with unrealistic distance cues or spatial artifacts when beyond the training range. These failures are further illustrated by audio examples provided in the demo page.

6 Ablation Analysis

The significance of each core component within the proposed method (GTW, AS, and WaveFit) is evaluated through ablation studies (Table 3). All three components demonstrably contribute to the system’s overall success. First, AS is critical for ZeroBAS performance. Its absence leads to substantial degradation in both MOS and Wave ℓ_2 error. Amplitude scaling between left and right channels creates a crucial perceptual difference, essential for accurate binaural audio modeling. GTW is the second most important component. Without GTW, left-right channel time differences become misaligned, resulting in increased Wave ℓ_2 error and decreased MOS. The WaveFit model, when removed in isolation, has a minimal impact on objective metrics but a significant negative impact on MOS which highlights the importance to generate high-quality speech. Interestingly, removing both AS and GTW while retaining WaveFit leads to improved MOS, albeit resulting in a monaural waveform played identically in both channels. In addition we tested the effects of architectural modifications within the WaveFit inference process. Decoding for five iterations and initializing with Gaussian noise, as in the original WaveFit implementation, resulted in poor audio quality. This is because the two channels remain independent, and playing them as a binaural recording produces an unaligned and noisy output. Furthermore, applying WaveFit to the monaural input first, followed by AS and GTW, yielded improved performance in terms of Phase ℓ_2 but compromised MOS and Amplitude ℓ_2 metric. Finally, we evaluated the effect of the number of WaveFit iterations. Increasing the number of iterations until 3 improves the objective metrics Wave ℓ_2 , Amplitude ℓ_2 and Phase ℓ_2 and improves MOS. After 3 iterations, quality is constant but there is no need to continue iterating.

7 Limitations

ZeroBAS uses an off-the-shelf neural vocoder which is conditioned on (log-mel) spectrogram features and no positional information which makes it difficult to condition towards a target phase spectrum. For this reason, our method struggles to directly and accurately process the phase information in binaural audio, leading to high Phase ℓ_2 error. Furthermore, our method does not encode or use any room or head shape information. We hypothesize that this fact helps our method generalize to new

rooms and acoustic environments, while still not being able to match the performance of supervised methods which are trained on a specific room and acoustic environment.

8 Conclusion

In this work, we presented a room-agnostic zero-shot method for binaural speech synthesis from monaural audio. Our results demonstrate that the method achieves perceptual performance comparable to supervised approaches on their in-distribution datasets. Furthermore, we introduce a novel dataset specifically designed to evaluate the generalization capabilities of monaural-to-binaural synthesis methods for out-of-distribution scenarios. On this dataset, our zero-shot method exhibits superior performance compared to supervised methods, highlighting its potential for real-world applications with diverse acoustic environments.

References

- S. Adavanne, A. Politis, J. Nikunen, and T. Virtanen. Sound event localization and detection of overlapping sources using convolutional recurrent neural networks. *IEEE J. Sel. Top. Signal Process.*, 13(1):34–48, 2019. URL <https://doi.org/10.1109/JSTSP.2018.2885636>.
- F. Baumgarte and C. Faller. Binaural cue coding - Part I: psychoacoustic fundamentals and design principles. *IEEE Trans. Speech Audio Process.*, 11(6):509–519, 2003. URL <https://doi.org/10.1109/TSA.2003.818109>.
- C. Chen, A. Richard, R. Shapovalov, V. K. Ithapu, N. Neverova, K. Grauman, and A. Vedaldi. Novel-view acoustic synthesis. In *IEEE/CVF Conference on Computer Vision and Pattern Recognition, CVPR 2023, Vancouver, BC, Canada, June 17-24, 2023*, pages 6409–6419. IEEE, 2023a. URL <https://doi.org/10.1109/CVPR52729.2023.00620>.
- M. Chen, K. Su, and E. Shlizerman. Be everywhere - hear everything (BEE): Audio scene reconstruction by sparse audio-visual samples. In *IEEE/CVF International Conference on Computer Vision, ICCV 2023, Paris, France, October 1-6, 2023*, pages 7819–7828. IEEE, 2023b. URL <https://doi.org/10.1109/ICCV51070.2023.00722>.
- N. Chen, Y. Zhang, H. Zen, R. J. Weiss, M. Norouzi, and W. Chan. WaveGrad: Estimating gradients for waveform generation. In *9th International Conference on Learning Representations, ICLR 2021, Virtual Event, Austria, May 3-7, 2021*. OpenReview.net, 2021. URL <https://openreview.net/forum?id=NsMLjcFa080>.
- R. Garg, R. Gao, and K. Grauman. Geometry-aware multi-task learning for binaural audio generation from video. In *32nd British Machine Vision Conference 2021, BMVC 2021, Online, November 22-25, 2021*, page 1. BMVA Press, 2021. URL <https://www.bmvc2021-virtualconference.com/assets/papers/1098.pdf>.
- I. D. Gebru, D. Markovic, A. Richard, S. Krenn, G. A. Butler, F. D. la Torre, and Y. Sheikh. Implicit HRTF modeling using temporal convolutional networks. In *IEEE International Conference on Acoustics, Speech and Signal Processing, ICASSP 2021, Toronto, ON, Canada, June 6-11, 2021*, pages 3385–3389. IEEE, 2021. URL <https://doi.org/10.1109/ICASSP39728.2021.9414750>.
- J. Ho, A. Jain, and P. Abbeel. Denoising diffusion probabilistic models. In *Advances in Neural Information Processing Systems 33, NeurIPS 2020, December 6-12, 2020, virtual*, 2020. URL <https://proceedings.neurips.cc/paper/2020/hash/4c5bcfec8584af0d967f1ab10179ca4b-Abstract.html>.
- W. Huang, D. Markovic, A. Richard, I. D. Gebru, and A. Menon. End-to-end binaural speech synthesis. In *Interspeech 2022, 23rd Annual Conference of the International Speech Communication Association, Incheon, Korea, 18-22 September 2022*, pages 1218–1222. ISCA, 2022. URL <https://doi.org/10.21437/Interspeech.2022-10603>.

- J. Kahn, M. Rivière, W. Zheng, E. Kharitonov, Q. Xu, P. Mazaré, J. Karadayi, V. Liptchinsky, R. Collobert, C. Fuegen, T. Likhomanenko, G. Synnaeve, A. Joulin, A. Mohamed, and E. Dupoux. Libri-Light: A benchmark for ASR with limited or no supervision. In *2020 IEEE International Conference on Acoustics, Speech and Signal Processing, ICASSP 2020, Barcelona, Spain, May 4-8, 2020*, pages 7669–7673. IEEE, 2020. URL <https://doi.org/10.1109/ICASSP40776.2020.9052942>.
- K. Kitamura and K. Itou. Binaural audio synthesis with the structured state space sequence model. In *2023 9th International Conference on Computer and Communications (ICCC)*, pages 1505–1509, 2023. URL <https://doi.org/10.1109/ICCC59590.2023.10507442>.
- Y. Koizumi, K. Yatabe, H. Zen, and M. Bacchiani. WaveFit: an Iterative and non-autoregressive neural vocoder based on fixed-point iteration. In *IEEE Spoken Language Technology Workshop, SLT 2022, Doha, Qatar, January 9-12, 2023*, pages 884–891. IEEE, 2022a. URL <https://doi.org/10.1109/SLT54892.2023.10022496>.
- Y. Koizumi, H. Zen, K. Yatabe, N. Chen, and M. Bacchiani. SpecGrad: Diffusion probabilistic model based neural vocoder with adaptive noise spectral shaping. In *Interspeech 2022, 23rd Annual Conference of the International Speech Communication Association, Incheon, Korea, 18-22 September 2022*, pages 803–807. ISCA, 2022b. URL <https://doi.org/10.21437/Interspeech.2022-301>.
- K. Kumar, R. Kumar, T. de Boissiere, L. Gestin, W. Z. Teoh, J. Sotelo, A. de Brébisson, Y. Bengio, and A. C. Courville. Melgan: Generative adversarial networks for conditional waveform synthesis. In *NeurIPS*, pages 14881–14892, 2019.
- G. Lafay, E. Benetos, and M. Lagrange. Sound event detection in synthetic audio: Analysis of the DCASE 2016 task results. In *2017 IEEE Workshop on Applications of Signal Processing to Audio and Acoustics, WASPAA 2017, New Paltz, NY, USA, October 15-18, 2017*, pages 11–15. IEEE, 2017. URL <https://doi.org/10.1109/WASPAA.2017.8169985>.
- J. W. Lee and K. Lee. Neural Fourier shift for binaural speech rendering. In *IEEE International Conference on Acoustics, Speech and Signal Processing ICASSP 2023, Rhodes Island, Greece, June 4-10, 2023*, pages 1–5. IEEE, 2023. URL <https://doi.org/10.1109/ICASSP49357.2023.10095685>.
- S. Lee, H. Choi, and K. Lee. Differentiable artificial reverberation. *IEEE ACM Trans. Audio Speech Lang. Process.*, 30:2541–2556, 2022. URL <https://doi.org/10.1109/TASLP.2022.3193298>.
- Y. Leng, Z. Chen, J. Guo, H. Liu, J. Chen, X. Tan, D. P. Mandic, L. He, X. Li, T. Qin, S. Zhao, and T. Liu. BinauralGrad: A two-stage conditional diffusion probabilistic model for binaural audio synthesis. In *Advances in Neural Information Processing Systems 35, NeurIPS 2022, New Orleans, LA, USA, November 28 - December 9, 2022*, 2022. URL http://papers.nips.cc/paper_files/paper/2022/hash/95f03faf3763e1b1ce2c3de62da8f090-Abstract-Conference.html.
- S. Li and J. Peissig. Measurement of head-related transfer functions: A review. *Applied Sciences*, 10(14):5014, 2020. URL <https://doi.org/10.3390/app10145014>.
- S. Liang, C. Huang, Y. Tian, A. Kumar, and C. Xu. AV-NeRF: Learning neural fields for real-world audio-visual scene synthesis. In *Advances in Neural Information Processing Systems 36, NeurIPS 2023, New Orleans, LA, USA, December 10 - 16, 2023*, 2023. URL http://papers.nips.cc/paper_files/paper/2023/hash/760dff0f9c0e9ed4d7e22918c73351d4-Abstract-Conference.html.
- J. Liu, Z. Ye, Q. Chen, S. Zheng, W. Wang, Q. Zhang, and Z. Zhao. DopplerBAS: Binaural audio synthesis addressing Doppler effect. In *Findings of the Association for Computational Linguistics: ACL 2023, Toronto, Canada, July 9-14, 2023*, pages 11905–11912. Association for Computational Linguistics, 2023. URL <https://doi.org/10.18653/v1/2023.findings-acl.753>.
- A. Luo, Y. Du, M. J. Tarr, J. Tenenbaum, A. Torralba, and C. Gan. Learning neural acoustic fields. In *Advances in Neural Information Processing Systems 35, NeurIPS 2022, New Orleans, LA, USA, November 28 - December 9, 2022*, 2022. URL http://papers.nips.cc/paper_files/paper/2022/hash/151f4dfc71f025ae387e2d7a4ea1639b-Abstract-Conference.html.

- K. K. Parida, S. Srivastava, and G. Sharma. Beyond mono to binaural: Generating binaural audio from mono audio with depth and cross modal attention. In *IEEE/CVF Winter Conference on Applications of Computer Vision, WACV 2022, Waikoloa, HI, USA, January 3-8, 2022*, pages 2151–2160. IEEE, 2022. URL <https://doi.org/10.1109/WACV51458.2022.00221>.
- A. Richard, D. Markovic, I. D. Gebru, S. Krenn, G. A. Butler, F. D. la Torre, and Y. Sheikh. Neural synthesis of binaural speech from mono audio. In *9th International Conference on Learning Representations, ICLR 2021, Virtual Event, Austria, May 3-7, 2021*. OpenReview.net, 2021. URL <https://openreview.net/forum?id=uAX8q61EVRu>.
- A. Richard, P. S. Dodds, and V. K. Ithapu. Deep impulse responses: Estimating and parameterizing filters with deep networks. In *IEEE International Conference on Acoustics, Speech and Signal Processing, ICASSP 2022, Virtual and Singapore, 23-27 May 2022*, pages 3209–3213. IEEE, 2022. URL <https://doi.org/10.1109/ICASSP43922.2022.9746135>.
- L. Savioja, J. Huopaniemi, T. Lokki, and R. Väänänen. Creating interactive virtual acoustic environments. *Journal of the Audio Engineering Society*, 47(9):675–705, 1999. URL <https://www.aes.org/e-lib/browse.cfm?elib=12095>.
- A. Somayazulu, C. Chen, and K. Grauman. Self-supervised visual acoustic matching. In *Advances in Neural Information Processing Systems 36, NeurIPS 2023, New Orleans, LA, USA, December 10 - 16, 2023*, 2023. URL http://papers.nips.cc/paper_files/paper/2023/hash/4cbec10b0cf25025e3f9fcfd943bb58c-Abstract-Conference.html.
- K. Sunder, J. He, E. Tan, and W. Gan. Natural sound rendering for headphones: Integration of signal processing techniques. *IEEE Signal Process. Mag.*, 32(2):100–113, 2015. URL <https://doi.org/10.1109/MSP.2014.2372062>.
- V. Välimäki, J. D. Parker, L. Savioja, J. O. S. III, and J. S. Abel. Fifty years of artificial reverberation. *IEEE Trans. Speech Audio Process.*, 20(5):1421–1448, 2012. URL <https://doi.org/10.1109/TASL.2012.2189567>.
- G. Wersényi. Representations of HRTFs using MATLAB: 2D and 3D plots of accurate dummy-head measurements. In *Proceedings of 20th International Congress on Acoustics, ICA 2010*, pages 1–6, 2010. URL https://www.acoustics.asn.au/conference_proceedings/ICA2010/cdrom-ICA2010/papers/p45.pdf.
- X. Xu, H. Zhou, Z. Liu, B. Dai, X. Wang, and D. Lin. Visually informed binaural audio generation without binaural audios. In *IEEE Conference on Computer Vision and Pattern Recognition, CVPR 2021, virtual, June 19-25, 2021*, pages 15485–15494. Computer Vision Foundation / IEEE, 2021. URL <https://doi.org/10.1109/CVPR46437.2021.01523>.
- X. Xu, D. Markovic, J. Sandakly, T. Keebler, S. Krenn, and A. Richard. Sounding bodies: Modeling 3D spatial sound of humans using body pose and audio. In *Advances in Neural Information Processing Systems 36, NeurIPS 2023, New Orleans, LA, USA, December 10 - 16, 2023*, 2023. URL http://papers.nips.cc/paper_files/paper/2023/hash/8c234d9c7e738a793947e0282c36eb95-Abstract-Conference.html.
- M. Yoshida, R. Togo, T. Ogawa, and M. Haseyama. Binauralization robust to camera rotation using 360° videos. In *IEEE International Conference on Acoustics, Speech and Signal Processing ICASSP 2023, Rhodes Island, Greece, June 4-10, 2023*, pages 1–5. IEEE, 2023. URL <https://doi.org/10.1109/ICASSP49357.2023.10096349>.
- P. Zahorik, D. S. Brungart, and A. W. Bronkhorst. Auditory distance perception in humans: A summary of past and present research. *ACTA Acustica united with Acustica*, 91(3):409–420, 2005.
- W. Zhang, P. N. Samarasinghe, H. Chen, and T. D. Abhayapala. Surround by sound: A review of spatial audio recording and reproduction. *Applied Sciences*, 7(5):532, 2017. URL <https://doi.org/10.3390/app7050532>.
- D. N. Zotkin, R. Duraiswami, and L. S. Davis. Rendering localized spatial audio in a virtual auditory space. *IEEE Trans. Multim.*, 6(4):553–564, 2004. URL <https://doi.org/10.1109/TMM.2004.827516>.

Appendix

A Proof of Lemma 1

A.1 Phase error:

Utilizing the definition of the phase error as presented Lemma 1 of [Richard et al., 2021]:

$$\mathbb{E}_Y \left(\mathcal{L}^{(\text{phase})}(Y, \hat{Y}) \right) = \frac{1}{2\pi} \int_{-\pi}^{\pi} \arccos \frac{\operatorname{Re} \left(\frac{\varepsilon}{|\hat{Y}|} \cdot e^{i\varphi} + 1 \right)}{\left| \frac{\varepsilon}{|\hat{Y}|} + e^{i\varphi} \right|} d\varphi \quad (6)$$

The integral over the phase φ can be evaluated by the following steps:

$$\mathbb{E}_Y \left(\mathcal{L}^{(\text{phase})}(Y, \hat{Y}) \right) = \quad (7)$$

$$= \frac{1}{2\pi} \int_{-\pi}^{\pi} \arccos \frac{\operatorname{Re} \left(\frac{\varepsilon}{|\hat{Y}|} \cdot e^{i\varphi} + 1 \right)}{\left| \frac{\varepsilon}{|\hat{Y}|} + e^{i\varphi} \right|} d\varphi \quad (8)$$

$$= \frac{1}{2\pi} \int_{-\pi}^{\pi} \arccos \frac{\operatorname{Re} \left(\frac{\varepsilon}{|\hat{Y}|} \cdot (\cos(\varphi) + i \cdot \sin(\varphi)) + 1 \right)}{\left| \frac{\varepsilon}{|\hat{Y}|} + \cos(\varphi) + i \cdot \sin(\varphi) \right|} d\varphi \quad (9)$$

$$= \frac{1}{2\pi} \int_{-\pi}^{\pi} \arccos \frac{\frac{\varepsilon \cdot \cos(\varphi)}{|\hat{Y}|} + 1}{\sqrt{\left(\frac{\varepsilon}{|\hat{Y}|} + \cos(\varphi) \right)^2 + \sin^2(\varphi)}} d\varphi \quad (10)$$

$$= \frac{1}{2\pi} \int_{-\pi}^{\pi} \arccos \frac{\frac{\varepsilon \cdot \cos(\varphi)}{|\hat{Y}|} + 1}{\sqrt{\left(\frac{\varepsilon}{|\hat{Y}|} \right)^2 + \frac{2\varepsilon \cdot \cos(\varphi)}{|\hat{Y}|} + 1}} d\varphi \quad (11)$$

$$= \frac{1}{2\pi} \int_{-\pi}^{\pi} \arccos \left[\left(\frac{\varepsilon \cdot \cos(\varphi)}{|\hat{Y}|} + 1 \right) \cdot \left(\frac{1}{\sqrt{\left(\frac{\varepsilon}{|\hat{Y}|} \right)^2 + \frac{2\varepsilon \cdot \cos(\varphi)}{|\hat{Y}|} + 1}} \right) \right] d\varphi \quad (12)$$

Assume that we are in high error regime, i.e. $\frac{\varepsilon}{|\hat{Y}|} \gg 1$:

$$\mathbb{E}_Y \left(\mathcal{L}^{(\text{phase})}(Y, \hat{Y}) \right) \approx \frac{1}{2\pi} \int_{-\pi}^{\pi} \arccos \left[\frac{\frac{\varepsilon}{|\hat{Y}|} \cos(\varphi)}{\sqrt{\left(\frac{\varepsilon}{|\hat{Y}|} \right)^2 + \frac{2\varepsilon \cdot \cos(\varphi)}{|\hat{Y}|} + 1}} \right] d\varphi \quad (13)$$

Since in the high-error regime where $\frac{\varepsilon}{|\hat{Y}|} \gg 1$ the constant term 1 in the numerator can be disregarded as negligible. Then $\mathbb{E}_Y \left(\mathcal{L}^{(\text{phase})}(Y, \hat{Y}) \right)$ can be written as:

$$\frac{1}{2\pi} \int_{-\pi}^{\pi} \arccos \left[\frac{\cos(\varphi)}{\sqrt{1 + \frac{2|\hat{Y}| \cdot \cos(\varphi)}{\varepsilon} + \left(\frac{|\hat{Y}|}{\varepsilon}\right)^2}} \right] d\varphi \quad (14)$$

$$\approx \frac{1}{2\pi} \int_{-\pi}^{\pi} \arccos \left[\frac{\cos(\varphi)}{\sqrt{1 + \frac{2|\hat{Y}| \cdot \cos(\varphi)}{\varepsilon}}} \right] d\varphi \quad (15)$$

$$\approx \frac{1}{2\pi} \int_{-\pi}^{\pi} \arccos \left[\cos(\varphi) \left(1 - \frac{|\hat{Y}| \cdot \cos(\varphi)}{\varepsilon} \right) \right] d\varphi \quad (16)$$

Since, in high error regime $\left(\frac{|\hat{Y}|}{\varepsilon}\right)^2 \ll 1$ and the Taylor series expansion employed is $\frac{1}{\sqrt{1+x}} \approx 1 - \frac{x}{2}$ where $x = \frac{2|\hat{Y}| \cdot \cos(\varphi)}{\varepsilon}$. Thus, $\mathbb{E}_Y \left(\mathcal{L}^{(\text{phase})}(Y, \hat{Y}) \right)$ can be expressed as:

$$\frac{1}{2\pi} \int_{-\pi}^{\pi} \arccos \left[\cos(\varphi) - \frac{|\hat{Y}|}{\varepsilon} \cdot \cos^2(\varphi) \right] d\varphi \quad (17)$$

$$= \frac{1}{2\pi} \int_{-\pi}^{\pi} \arccos \left[\cos(\varphi) - \frac{|\hat{Y}|}{\varepsilon} \cdot \left(\frac{\cos(2\varphi) + 1}{2} \right) \right] d\varphi \quad (18)$$

$$= \frac{1}{2\pi} \int_{-\pi}^{\pi} \arccos \left[\cos(\varphi) - \frac{|\hat{Y}|}{\varepsilon} \cdot \frac{\cos(2\varphi)}{2} - \frac{|\hat{Y}|}{2\varepsilon} \right] d\varphi \quad (19)$$

$$\approx \frac{1}{2\pi} \int_{-\pi}^{\pi} \arccos \left[\cos(\varphi) - \frac{|\hat{Y}|}{\varepsilon} \cdot \frac{\cos(2\varphi)}{2} \right] d\varphi \quad (20)$$

where $\frac{|\hat{Y}|}{\varepsilon}$ can be neglected as $\frac{|\hat{Y}|}{\varepsilon} \ll 1$. The Taylor Series expansion $\arccos(x) \approx \frac{\pi}{2} - x$ is used, where $x = \cos(\varphi) - \frac{|\hat{Y}|}{\varepsilon} \cdot \frac{\cos(2\varphi)}{2}$. Therefore, $\mathbb{E}_Y \left(\mathcal{L}^{(\text{phase})}(Y, \hat{Y}) \right)$ is equal to:

$$\frac{1}{2\pi} \int_{-\pi}^{\pi} \frac{\pi}{2} - \cos(\varphi) + \frac{|\hat{Y}|}{\varepsilon} \cdot \frac{\cos(2\varphi)}{2} d\varphi \quad (21)$$

$$= \frac{1}{2\pi} \int_{-\pi}^{\pi} \left(\frac{\pi}{2} - \cos(\varphi) + \frac{|\hat{Y}|}{\varepsilon} \cdot \frac{\cos(2\varphi)}{2} \right) d\varphi \quad (22)$$

$$= \frac{1}{2\pi} \int_{-\pi}^{\pi} \frac{\pi}{2} d\varphi + \frac{1}{2\pi} \int_{-\pi}^{\pi} \cos(\varphi) d\varphi + \frac{1}{2\pi} \int_{-\pi}^{\pi} \frac{|\hat{Y}|}{\varepsilon} \cdot \frac{\cos(2\varphi)}{2} d\varphi \quad (23)$$

$$= \frac{\pi}{2} + 0 + 0 = \frac{\pi}{2} \quad (24)$$

Overall, the phase error is expressed as:

$$\mathbb{E}_Y \left(\mathcal{L}^{(\text{phase})}(Y, \hat{Y}) \right) \approx \frac{\pi}{2}. \quad (25)$$

□

A.2 Amplitude error:

We can then start from the definition of the amplitude error from lemma 1 in [Richard et al., 2021] and solve the integral:

$$\mathbb{E}_Y \left(\mathcal{L}^{(\text{amp})}(Y, \hat{Y}) \right) = \frac{|\hat{Y}|}{2\pi} \int_{-\pi}^{\pi} \left| \frac{\varepsilon}{|\hat{Y}|} + e^{i\varphi} - 1 \right| d\varphi \quad (26)$$

$$= \frac{|\hat{Y}|}{2\pi} \int_{-\pi}^{\pi} \left| \sqrt{\left(\frac{\varepsilon}{|\hat{Y}|} + \cos \varphi\right)^2 + \sin^2 \varphi} - 1 \right| d\varphi \quad (27)$$

$$= \frac{|\hat{Y}|}{2\pi} \int_{-\pi}^{\pi} \left| \sqrt{\left(\frac{\varepsilon}{|\hat{Y}|}\right)^2 + \frac{2\varepsilon \cos \varphi}{|\hat{Y}|} + \cos^2 \varphi + \sin^2 \varphi} - 1 \right| d\varphi \quad (28)$$

$$= \frac{|\hat{Y}|}{2\pi} \int_{-\pi}^{\pi} \left| \sqrt{\left(\frac{\varepsilon}{|\hat{Y}|}\right)^2 + \frac{2\varepsilon \cos \varphi}{|\hat{Y}|} + 1} - 1 \right| d\varphi \quad (29)$$

$$= \frac{|\hat{Y}|}{2\pi} \int_{-\pi}^{\pi} \left| \frac{\varepsilon}{|\hat{Y}|} \sqrt{1 + \frac{2|\hat{Y}| \cos \varphi}{\varepsilon} + \left(\frac{|\hat{Y}|}{\varepsilon}\right)^2} - 1 \right| d\varphi \quad (30)$$

$$\stackrel{(*)}{\approx} \frac{|\hat{Y}|}{2\pi} \int_{-\pi}^{\pi} \left| \frac{\varepsilon}{|\hat{Y}|} \sqrt{1 + \frac{2|\hat{Y}| \cos \varphi}{\varepsilon}} - 1 \right| d\varphi \quad (31)$$

$$\stackrel{(**)}{\approx} \frac{|\hat{Y}|}{2\pi} \int_{-\pi}^{\pi} \left| \frac{\varepsilon}{|\hat{Y}|} \left(1 + \frac{1}{2} \cdot \frac{2|\hat{Y}| \cos \varphi}{\varepsilon} \right) - 1 \right| d\varphi \quad (32)$$

$$= \frac{|\hat{Y}|}{2\pi} \int_{-\pi}^{\pi} \left| \frac{\varepsilon}{|\hat{Y}|} + \cos \varphi - 1 \right| d\varphi \quad (33)$$

$$\stackrel{(***)}{\approx} \frac{|\hat{Y}|}{2\pi} \int_{-\pi}^{\pi} \left(\frac{\varepsilon}{|\hat{Y}|} + \cos \varphi \right) d\varphi \quad (34)$$

$$= \frac{|\hat{Y}|}{2\pi} \cdot \frac{\varepsilon}{|\hat{Y}|} \cdot 2\pi + \frac{|\hat{Y}|}{2\pi} \int_{-\pi}^{\pi} \cos \varphi d\varphi \quad (35)$$

$$= \varepsilon + 0 = \varepsilon \quad (36)$$

In the above derivation, the following approximations were employed, under the assumption that $\frac{\varepsilon}{|\hat{Y}|} \gg 1$:

1. (*) Removing the term $\left(\frac{|\hat{Y}|}{\varepsilon}\right)^2$ since by the assumption it is negligible.
2. (**) Using the Taylor Series expansion: $\sqrt{1+x} \approx 1 + \frac{x}{2}$ where $x = \frac{2|\hat{Y}| \cdot \cos(\varphi)}{\varepsilon}$
3. (***) Removing the term 1 and the $|\cdot|$ function since the overall integrand is dominated by the term $\frac{\varepsilon}{|\hat{Y}|}$.

Overall, the amplitude error is expressed as - $\mathbb{E}_Y \left(\mathcal{L}^{(\text{amp})}(Y, \hat{Y}) \right) \approx \varepsilon$. \square

B Low Error Regime - Lemma 2

Lemma 2. Let $\hat{Y} \in \mathbb{C}$, and let there be a ball of complex numbers with distance ε from \hat{Y} such that $Y \in \mathbb{B}_\varepsilon = \{Y \in \mathbb{C} : |Y - \hat{Y}| = \varepsilon\}$. Assuming a low error regime where $\frac{\varepsilon}{|\hat{Y}|} \ll 1$, then the expected amplitude and phase errors are:

$$\mathbb{E}_Y \left(\mathcal{L}^{(\text{phase})}(Y, \hat{Y}) \right) \approx \left(\frac{\pi}{2} - 1 \right) + \frac{\varepsilon^2}{2|\hat{Y}|^2}, \quad (37)$$

$$\mathbb{E}_Y \left(\mathcal{L}^{(\text{amp})}(Y, \hat{Y}) \right) \approx \begin{cases} \varepsilon - \frac{\pi^2 |\hat{Y}| \varepsilon}{3(2|\hat{Y}| + \varepsilon)}, & \frac{\varepsilon}{|\hat{Y}|} \geq \frac{\pi^2}{2} - 1 \\ \frac{\pi^2 |\hat{Y}| \varepsilon}{3(2|\hat{Y}| + \varepsilon)} - \varepsilon + \frac{4\varepsilon \sqrt{\frac{2|\hat{Y}| + \varepsilon}{|\hat{Y}| \varepsilon}}}{3\pi}, & \frac{\varepsilon}{|\hat{Y}|} \leq \frac{\pi^2}{2} - 1. \end{cases} \quad (38)$$

Proof. Angular phase error: We can then start from the definition of the phase error from lemma 1 in [Richard et al., 2021] and solve the integral:

$$\mathbb{E}_Y \left(\mathcal{L}^{(\text{phase})}(Y, \hat{Y}) \right) = \frac{1}{2\pi} \int_{-\pi}^{\pi} \arccos \frac{\operatorname{Re} \left(\frac{\varepsilon}{|\hat{Y}|} \cdot e^{i\varphi} + 1 \right)}{\left| \frac{\varepsilon}{|\hat{Y}|} + e^{i\varphi} \right|} d\varphi \quad (39)$$

$$= \frac{1}{2\pi} \int_{-\pi}^{\pi} \arccos \frac{\operatorname{Re} \left(\frac{\varepsilon}{|\hat{Y}|} \cdot (\cos(\varphi) + i \cdot \sin(\varphi)) + 1 \right)}{\left| \frac{\varepsilon}{|\hat{Y}|} + \cos(\varphi) + i \cdot \sin(\varphi) \right|} d\varphi \quad (40)$$

$$= \frac{1}{2\pi} \int_{-\pi}^{\pi} \arccos \frac{\frac{\varepsilon \cdot \cos(\varphi)}{|\hat{Y}|} + 1}{\sqrt{\left(\frac{\varepsilon}{|\hat{Y}|} + \cos(\varphi) \right)^2 + \sin^2(\varphi)}} d\varphi \quad (41)$$

Since $\cos^2(\varphi) + \sin^2(\varphi) = 1$, the phase error $\mathbb{E}_Y \left(\mathcal{L}^{(\text{phase})}(Y, \hat{Y}) \right)$ can be expressed as:

$$= \frac{1}{2\pi} \int_{-\pi}^{\pi} \arccos \frac{\frac{\varepsilon \cdot \cos(\varphi)}{|\hat{Y}|} + 1}{\sqrt{\left(\frac{\varepsilon}{|\hat{Y}|} \right)^2 + \frac{2\varepsilon \cdot \cos(\varphi)}{|\hat{Y}|} + 1}} d\varphi \quad (42)$$

$$= \frac{1}{2\pi} \int_{-\pi}^{\pi} \arccos \left[\left(\frac{\varepsilon \cdot \cos(\varphi)}{|\hat{Y}|} + 1 \right) \cdot \left(\frac{1}{\sqrt{\left(\frac{\varepsilon}{|\hat{Y}|} \right)^2 + \frac{2\varepsilon \cdot \cos(\varphi)}{|\hat{Y}|} + 1}} \right) \right] d\varphi \quad (43)$$

$$\approx \frac{1}{2\pi} \int_{-\pi}^{\pi} \arccos \left(\frac{\varepsilon \cdot \cos(\varphi)}{|\hat{Y}|} + 1 \right) \cdot \left(1 - \frac{1}{2} \left(\frac{\varepsilon}{|\hat{Y}|} \right)^2 - \frac{\varepsilon \cdot \cos(\varphi)}{|\hat{Y}|} \right) d\varphi \quad (44)$$

$$\approx \frac{1}{2\pi} \int_{-\pi}^{\pi} \arccos \left(1 + \frac{\varepsilon \cdot \cos(\varphi)}{|\hat{Y}|} \right) \cdot \left(1 - \frac{\varepsilon \cdot \cos(\varphi)}{|\hat{Y}|} \right) d\varphi \quad (45)$$

Utilizing Taylor expansion $\frac{1}{\sqrt{1+x}} \approx 1 - \frac{x}{2}$ when $x = \left(\frac{\varepsilon}{|\hat{Y}|} \right)^2 + \frac{2\varepsilon \cdot \cos(\varphi)}{|\hat{Y}|}$ and removing the term $\frac{1}{2} \left(\frac{\varepsilon}{|\hat{Y}|} \right)^2$ since by our assumption it is negligible. Therefore, the phase error $\mathbb{E}_Y \left(\mathcal{L}^{(\text{phase})}(Y, \hat{Y}) \right)$ can be written as:

$$= \frac{1}{2\pi} \int_{-\pi}^{\pi} \arccos \left(1 - \frac{\varepsilon^2 \cdot \cos^2(\varphi)}{|\hat{Y}|^2} \right) d\varphi \quad (46)$$

$$\stackrel{(***)}{\approx} \frac{1}{2\pi} \int_{-\pi}^{\pi} \left(\frac{\pi}{2} - 1 + \frac{\varepsilon^2 \cdot \cos^2(\varphi)}{|\hat{Y}|^2} \right) d\varphi \quad (47)$$

Since $\arccos(x) \approx \frac{\pi}{2} - x$ where $x = 1 - \frac{\varepsilon^2 \cdot \cos^2 \varphi}{|\hat{Y}|^2}$. Then, the phase error $\mathbb{E}_Y \left(\mathcal{L}^{(\text{phase})}(Y, \hat{Y}) \right)$ can be expressed as:

$$= \left(\frac{\pi}{2} - 1 \right) + \frac{1}{2\pi} \int_{-\pi}^{\pi} \frac{\varepsilon^2 \cdot \cos^2(\varphi)}{|\hat{Y}|^2} d\varphi \quad (48)$$

$$= \left(\frac{\pi}{2} - 1 \right) + \frac{\varepsilon^2}{2\pi|\hat{Y}|^2} \int_{-\pi}^{\pi} \cos^2(\varphi) d\varphi \quad (49)$$

$$= \left(\frac{\pi}{2} - 1 \right) + \frac{\varepsilon^2}{2\pi|\hat{Y}|^2} \int_{-\pi}^{\pi} \cos^2(\varphi) d\varphi \quad (50)$$

$$= \left(\frac{\pi}{2} - 1 \right) + \frac{\varepsilon^2}{2\pi|\hat{Y}|^2} \left[\frac{\varphi}{2} + \frac{\sin(2\varphi)}{4} \right] \Big|_{-\pi}^{\pi} \quad (51)$$

$$= \left(\frac{\pi}{2} - 1 \right) + \frac{\varepsilon^2}{2|\hat{Y}|^2} \quad (52)$$

Amplitude error: We can then start from the definition of the amplitude error from lemma 1 in [Richard et al., 2021] and solve the integral:

$$\mathbb{E}_Y \left(\mathcal{L}^{(\text{amp})}(Y, \hat{Y}) \right) = \frac{|\hat{Y}|}{2\pi} \int_{-\pi}^{\pi} \left| \frac{\varepsilon}{|\hat{Y}|} + e^{i\varphi} - 1 \right| d\varphi \quad (53)$$

$$= \frac{|\hat{Y}|}{2\pi} \int_{-\pi}^{\pi} \left| \sqrt{\left(\frac{\varepsilon}{|\hat{Y}|} + \cos \varphi\right)^2 + \sin^2 \varphi} - 1 \right| d\varphi \quad (54)$$

$$= \frac{|\hat{Y}|}{2\pi} \int_{-\pi}^{\pi} \left| \sqrt{\left(\frac{\varepsilon}{|\hat{Y}|}\right)^2 + \frac{2\varepsilon \cos \varphi}{|\hat{Y}|} + \cos^2 \varphi + \sin^2 \varphi} - 1 \right| d\varphi \quad (55)$$

$$= \frac{|\hat{Y}|}{2\pi} \int_{-\pi}^{\pi} \left| \sqrt{\left(\frac{\varepsilon}{|\hat{Y}|}\right)^2 + \frac{2\varepsilon \cos \varphi}{|\hat{Y}|} + 1} - 1 \right| d\varphi \quad (56)$$

$$= \frac{|\hat{Y}|}{2\pi} \int_{-\pi}^{\pi} \left| \sqrt{\left(\frac{\varepsilon}{|\hat{Y}|}\right)^2 + 1 + \frac{2\varepsilon \cos \varphi}{|\hat{Y}|}} - 1 \right| d\varphi \quad (57)$$

$$\approx^* \frac{|\hat{Y}|}{2\pi} \int_{-\pi}^{\pi} \left| \sqrt{\left(\frac{\varepsilon}{|\hat{Y}|}\right)^2 + 1 + \frac{2\varepsilon}{|\hat{Y}|} - \frac{\frac{2\varepsilon\varphi^2}{|\hat{Y}|}}{4\sqrt{\left(\frac{\varepsilon}{|\hat{Y}|}\right)^2 + 1 + \frac{2\varepsilon}{|\hat{Y}|}}} - 1 \right| d\varphi \quad (58)$$

$$= \frac{|\hat{Y}|}{2\pi} \int_{-\pi}^{\pi} \left| 1 + \frac{\varepsilon}{|\hat{Y}|} - \frac{\frac{2\varepsilon\varphi^2}{|\hat{Y}|}}{4\left(1 + \frac{\varepsilon}{|\hat{Y}|}\right)} - 1 \right| d\varphi \quad (59)$$

$$= \frac{|\hat{Y}|}{2\pi} \int_{-\pi}^{\pi} \left| \frac{\varepsilon}{|\hat{Y}|} - \frac{\frac{2\varepsilon\varphi^2}{|\hat{Y}|}}{4\left(1 + \frac{\varepsilon}{|\hat{Y}|}\right)} \right| d\varphi \quad (60)$$

$$= \frac{|\hat{Y}|}{2\pi} \cdot \frac{\varepsilon}{|\hat{Y}|} \int_{-\pi}^{\pi} \left| 1 - \frac{2\varphi^2}{4\left(1 + \frac{\varepsilon}{|\hat{Y}|}\right)} \right| d\varphi \quad (61)$$

$$= \frac{\varepsilon}{2\pi} \int_{-\pi}^{\pi} \left| 1 - \frac{\varphi^2}{2\left(1 + \frac{\varepsilon}{|\hat{Y}|}\right)} \right| d\varphi \quad (62)$$

$$= \frac{\varepsilon}{2\pi} \frac{1}{2\left(1 + \frac{\varepsilon}{|\hat{Y}|}\right)} \int_{-\pi}^{\pi} \left| 2\left(1 + \frac{\varepsilon}{|\hat{Y}|}\right) - \varphi^2 \right| d\varphi \quad (63)$$

We can then write

$$a = 2\left(1 + \frac{\varepsilon}{2|\hat{Y}|}\right), \frac{\varepsilon}{2a\pi} \int_{-\pi}^{\pi} |a - \varphi^2| d\varphi \quad (64)$$

And thus re-write the amplitude error as:

$$\mathbb{E}_Y \left(\mathcal{L}^{(\text{amp})}(Y, \hat{Y}) \right) = \frac{\varepsilon}{2a\pi} \int_{-\pi}^{\pi} |a - \varphi^2| d\varphi \quad (65)$$

The final error function will be a split function between $a > \pi^2$ and $a \leq \pi^2$. For $a > \pi^2$ we write:

$$\mathbb{E}_Y \left(\mathcal{L}^{(\text{amp})}(Y, \hat{Y}) \right) = \frac{\varepsilon}{2a\pi} \int_{-\pi}^{\pi} |a - \varphi^2| d\varphi \quad (66)$$

$$= \frac{\varepsilon}{2a\pi} \left(a\varepsilon - \frac{\varepsilon^3}{3} \right) \Big|_{-\pi}^{\pi} = \frac{\varepsilon}{2a\pi} \left(2\pi a - \frac{2\pi^3}{3} \right) \quad (67)$$

$$= \varepsilon \left(1 - \frac{\pi^2}{3a} \right) = \varepsilon - \frac{\varepsilon\pi^2}{3a} \quad (68)$$

$$= \varepsilon - \frac{\varepsilon\pi^2}{6 \left(1 + \frac{\varepsilon}{2|\hat{Y}|} \right)} = \varepsilon - \frac{\pi^2}{6 \left(\frac{1}{\varepsilon} + \frac{1}{2|\hat{Y}|} \right)} \quad (69)$$

$$= \varepsilon - \frac{\pi^2}{6 \left(\frac{2|\hat{Y}| + \varepsilon}{2|\hat{Y}|\varepsilon} \right)} = \varepsilon - \frac{\pi^2 |\hat{Y}| \varepsilon}{3(2|\hat{Y}| + \varepsilon)} \quad (70)$$

For $a \leq \pi^2$ we can write:

$$\mathbb{E}_Y \left(\mathcal{L}^{(\text{amp})}(Y, \hat{Y}) \right) = \frac{\varepsilon}{2a\pi} \int_{-\pi}^{\pi} |a - \varphi^2| d\varphi \quad (71)$$

$$= \frac{\varepsilon}{2a\pi} \left[\int_{-\pi}^{-\sqrt{a}} (\varphi^2 - a) d\varphi + \int_{-\sqrt{a}}^{\sqrt{a}} (a - \varphi^2) d\varphi + \int_{\sqrt{a}}^{\pi} (\varphi^2 - a) d\varphi \right] \quad (72)$$

$$= \frac{\varepsilon}{2a\pi} \left[\int_{-\sqrt{a}}^{\sqrt{a}} (a - \varphi^2) d\varphi + 2 \int_{\sqrt{a}}^{\pi} (\varphi^2 - a) d\varphi \right] \quad (73)$$

$$= \frac{\varepsilon}{2a\pi} \left[\left(a\varphi - \frac{\varphi^3}{3} \right) \Big|_{-\sqrt{a}}^{\sqrt{a}} + 2 \left(\frac{\varphi^3}{3} - a\varphi \right) \Big|_{\sqrt{a}}^{\pi} \right] \quad (74)$$

$$= \frac{\varepsilon}{2a\pi} \left[2 \left(a^{3/2} - \frac{a^{3/2}}{3} \right) + 2 \left(\frac{\pi^3 - a^{3/2}}{3} - a(\pi - \sqrt{a}) \right) \right] \quad (75)$$

$$= \frac{\varepsilon}{2a\pi} \left[2 \left(a^{3/2} - \frac{a^{3/2}}{3} \right) + 2 \left(\frac{\pi^3 - a^{3/2}}{3} - a(\pi - \sqrt{a}) \right) \right] \quad (76)$$

$$= \frac{\varepsilon}{2a\pi} \left[\frac{2\pi^3}{3} - 2\pi a + \frac{8a^{3/2}}{3} \right] \quad (77)$$

$$= \varepsilon \left[\frac{\pi^2}{3a} - 1 + \frac{4a^{1/2}}{3\pi} \right] \quad (78)$$

$$= \frac{\varepsilon\pi^2}{3a} - \varepsilon + \frac{4a^{1/2}\varepsilon}{3\pi} \quad (79)$$

$$= \frac{\varepsilon\pi^2}{6 \left(1 + \frac{\varepsilon}{2|\hat{Y}|} \right)} - \varepsilon + \frac{4\varepsilon \sqrt{2 \left(1 + \frac{\varepsilon}{2|\hat{Y}|} \right)}}{3\pi} \quad (80)$$

$$= \frac{\pi^2}{6 \left(\frac{2|\hat{Y}| + \varepsilon}{2|\hat{Y}|\varepsilon} \right)} - \varepsilon + \frac{4\varepsilon \sqrt{2 \left(\frac{2|\hat{Y}| + \varepsilon}{2|\hat{Y}|\varepsilon} \right)}}{3\pi} \quad (81)$$

$$= \frac{\pi^2 |\hat{Y}| \varepsilon}{3(2|\hat{Y}| + \varepsilon)} - \varepsilon + \frac{4\varepsilon \sqrt{\frac{2|\hat{Y}| + \varepsilon}{|\hat{Y}|\varepsilon}}}{3\pi} \quad (82)$$

Finally, we can merge the results from both the phase and amplitude errors to get

$$\mathbb{E}_Y \left(\mathcal{L}^{(\text{phase})}(Y, \hat{Y}) \right) \approx \left(\frac{\pi}{2} - 1 \right) + \frac{\varepsilon^2}{2|\hat{Y}|^2} \quad (83)$$

$$\mathbb{E}_Y \left(\mathcal{L}^{(\text{amp})}(Y, \hat{Y}) \right) \approx \begin{cases} \varepsilon - \frac{\pi^2 |\hat{Y}| \varepsilon}{3(2|\hat{Y}| + \varepsilon)} & , 2 \left(1 + \frac{\varepsilon}{|\hat{Y}|} \right) > \pi^2 \\ \frac{\pi^2 |\hat{Y}| \varepsilon}{3(2|\hat{Y}| + \varepsilon)} - \varepsilon + \frac{4\varepsilon \sqrt{\frac{2|\hat{Y}| + \varepsilon}{|\hat{Y}| \varepsilon}}}{3\pi} & , 2 \left(1 + \frac{\varepsilon}{|\hat{Y}|} \right) \leq \pi^2 \end{cases} \quad (84)$$

□

C Broader impacts

The proposed method employs a novel approach for enhancing mono audio signals into binaural audio. This technique has the potential to significantly improve the audio experience in augmented reality (AR) and virtual reality (VR) applications by creating a more immersive and realistic soundscape. The enhanced spatial audio cues generated by the proposed method can contribute to a heightened sense of presence and immersion within virtual environments. Additionally, the proposed method for transforming mono audio to binaural audio carries the potential for misuse in audio deepfake applications, where it could be employed to enhance the perceived realism and naturalness of manipulated audio through the introduction of artificially generated spatial cues.

D Mean Opinion Score (MOS) and MUSHRA experiments

To assess subjective quality, we gathered mean opinion scores (MOS) specifically focusing on the dimension of naturalness. Human evaluators were asked to rate the perceived naturalness of speech samples on a scale of 1 to 5, where 1 represented poor quality and 5 represented excellent quality. Each experiment involved 50 randomly selected samples per method, and each sample was evaluated 5 times by different raters. A minimum of 30 raters participated in each experiment. Moreover, in the MUSHRA (Multiple Stimuli with Hidden Reference and Anchor) evaluation, each question initially presents binaural recordings from the test set as a reference. Human raters are then asked to score the similarity of the model outputs to the reference on a scale from 0 to 100. The sample set includes a hidden reference serving as a high anchor, with the model outputs displayed in a random order. For this evaluation, we used 50 random samples from each method.

Table 4: Full MUSHRA results for the Binarual Speech Dataset

TYPE	MODEL	MUSHRA (\uparrow)
ZERO-SHOT	ZEROBAS (OURS)	70.46 \pm 7.14
SUPERVISED	WARPNET	74.57 \pm 7.01
	BINAURALGRAD	68.40 \pm 8.99
	NFS	61.47 \pm 9.36
-	GROUND TRUTH	95.37 \pm 3.53

Table 5: Full MUSHRA results for the TUT Mono to Binaural Dataset

TYPE	MODEL	MUSHRA (\uparrow)
ZERO-SHOT	ZEROBAS (OURS)	79.25 \pm 2.69
SUPERVISED	WARPNET	66.71 \pm 3.61
	BINAURALGRAD	36.35 \pm 5.84
	NFS	54.73 \pm 4.88
-	GROUND TRUTH	97.59 \pm 2.19